ADVANCED FUNCTIONAL MATERIALS
www.afm-journal.de

Direct Observation of Conducting Nanofilaments in Graphene-Oxide-Resistive Switching Memory

Sung Kyu Kim, Jong Yoon Kim, Sung-Yool Choi, Jeong Yong Lee,* and Hu Young Jeong**

Determining the presence of conducting filaments in resistive random access memory with nanoscale thin films is vital to unraveling resistive switching mechanisms. Bistable resistive switching within graphene-oxide (GO)-based resistive memory devices, recently developed by many research groups, has been generally explained by the formation and rupture of conducting filaments induced by the diffusion of metal or oxygen ions. Using a low-voltage spherical aberration-corrected transmission electron microscopy (TEM), we directly observe metallic nanofilaments formed at the amorphous top interface layer with the application of external voltages in an Al/GO/Al memory system. Atomic-resolution TEM images acquired at an acceleration voltage of 80 kV clearly show that the conducting nanofilaments are composed of nano-sized aluminum crystalline within the amorphous top interface layer after applying a negative bias (ON state). Simultaneously, we observe the change in the crystallinity of GO films by the back-diffusion of oxygen ions. The oxygen-deficient regions are clearly confirmed by energy-filtered TEM oxygen elemental mapping. This work could provide strong evidence to confirm the resistive switching mechanism previously suggested by our group.

1. Introduction

Resistive random access memory (RRAM) has emerged as an excellent candidate among next-generation nonvolatile memory (NVM) devices for overcoming the physical limitations of conventional charge-based memory devices due to its simple structure, high density, low power consumption, and fast switching speed.[1] To date, versatile resistive switching phenomena have been reported in various insulating or semiconducting materials, including binary transition metal oxides (NiO, TiO_2, Ta_2O_5, ZnO, and HfO_2),[2–7] perovskite oxides,[8] solid electrolytes,[9] organic materials,[10] and amorphous Si.[11]

Recently, carbon-based materials such as carbon nanotubes,[12,13] graphene-like conductive carbon,[14] and amorphous carbon[15,16] have also been considered as a potential element for resistance-change materials. Among these, graphene oxide (GO), a graphene sheet decorated with oxygen groups (epoxide, hydroxyl, and carboxyl) on both sides, is one of the most promising candidates owing to its easy methods such as drop casting, spin coating, Langmuir–Blodgett (LB) deposition, and vacuum filtration required for the fabrication of uniform thin films.[17] Besides, the switching properties of GO thin films can be tuned by changing their chemical functionalities through a reduction process[18] or by mixing with other materials such as polymers,[19,20] nanoparticles,[21] and MoS_2.[22] Although various GO-based memory devices have been suggested by research groups,[23–28] the exact mechanism of bistable resistive switching behavior in GO thin films is still not fully understood.

Previously, our group reported the development of a flexible nonvolatile memory device based on spin-casted GO thin films.[29] We presented the resistive switching mechanism as the formation and rupture of conducting nanofilaments formed at the amorphous top interface layer (TIL) between a GO thin film and an Al top electrode. To verify a microscopic model of this mechanism, it is crucial to directly observe the existence of conducting filaments.

Herein, we report on the direct visualization of nanoscale metallic filaments formed at the amorphous TIL during the set process. Using a spherical-aberration-corrected transmission electron microscope (TEM) operated at 80 kV, we obtained cross-sectional TEM images of GO thin films sandwiched between two Al electrodes. A quantitative calculation of the structural changes in the GO thin films after top electrode deposition was achieved using the radial distribution function (RDF) of fast Fourier transform (FFT) patterns acquired from the atomic-resolution TEM images. In addition, we used atomic-resolution TEM and energy-filtered TEM (EFTEM) elemental mapping to identify the origin of the nanoscale metallic filaments induced

S. K. Kim, Prof. J. Y. Lee
Department of Materials Science and Engineering
KAIST
Daejeon 34141, South Korea
E-mail: j.y.lee@kaist.ac.kr
J. Y. Kim, Prof. S.-Y. Choi
Graphene Research Center and School
of Electrical Engineering
KAIST
Daejeon 34141 South Korea
E-mail: sungyool.choi@kaist.ac.kr
Prof. J. Y. Lee
Center for Nanomaterials and Chemical Reactions
Institute for Basic Science (IBS)
Daejeon 34047, South Korea
Prof. H. Y. Jeong
UNIST Central Research Facilities (UCRF) and School
of Materials Science and Engineering
UNIST
Ulsan 44919, South Korea
E-mail: hulex@unist.ac.kr

DOI: 10.1002/adfm.201502734

by negative bias on the TIL. The present study provides a basis for addressing the reaction phenomena between metal and nanoscale GO thin films and interpreting the bipolar resistive switching behaviors of Al/GO/Al memory devices.

2. Results and Discussion

A GO solution was successfully synthesized using a modified Hummers method.[30–32] The size of GO sheets is generally dependent on the synthesis method. In our case, sheets were formed that were less than a few hundred nanometers, as seen in the SEM image of GO nanoflakes dispersed on an Si substrate (**Figure 1**c). In order to characterize the crystal structure of spin-coated GO films on an Al bottom electrode, GO thin films were transferred to an Au quantifoil TEM grid after etching the Al electrode using a solution of sodium persulfate ($Na_2S_2O_8$, at a concentration of 0.1 g in 1 mL of water) and rinsing with deionized water.[33] A scanning TEM (STEM) annular dark field (ADF) image (Figure 1d) shows that the film is uniformly and densely overlapped with nanoscale GO sheets. Each sheet is randomly oriented as confirmed by the selective area electron diffraction pattern of a ring (shown in the left inset of Figure 1d). An atomic-resolution TEM image (Figure S1, Supporting Information) indicates that a significant number of defects in the carbon network were induced by the mechanical exfoliation and chemical oxidation process.[34] The chemical state of the GO films was also examined by infrared (IR) spectra (Figure S2, Supporting Information) and electron energy loss spectroscopy (EELS). From the IR spectra, we observed the decoration of the GO films with oxygen-containing groups such as epoxide, hydroxyl, carbonyl, and carboxyl. Figure 1e shows the C and O K-edge spectra obtained from the GO films in Figure 1d. The C K-edge has two main peaks, which represent the electron transitions from the K-shell to the π^* states at 285.8 eV and to the σ^* states at 293.3 eV, respectively. Compared to perfect graphene, a weaken σ^* peak represents a disorder in the carbon hexagonal lattice structure due to the oxidation process.[35] In addition, O K-edge EELS spectra at 542.3 eV clearly verify the existence of oxygen ions in the GO films.

The inset of Figure 1a is a schematic illustration of our GO-based cross-bar RRAM device. We fabricated 5 × 5 memory arrays with the GO films sandwiched between two Al electrodes. Sequential high-resolution TEM (HRTEM) images of the stacked thin films are shown in Figure S3 in the Supporting Information. A current–voltage (*I–V*) curve of Al/GO/Al device shows conventional bipolar resistive switching behavior, as shown in Figure 1a. The ON state was formed by applying a negative bias to the top electrode, and a rapid current increase indicates the formation of conducting filaments (Figure S4, Supporting Information). A reverse bias was applied to the top electrode to return to the OFF state. As we previously reported, this resistive switching behavior can be explained by the reversible movement of negatively charged oxygen ions between the TIL and GO thin films. A

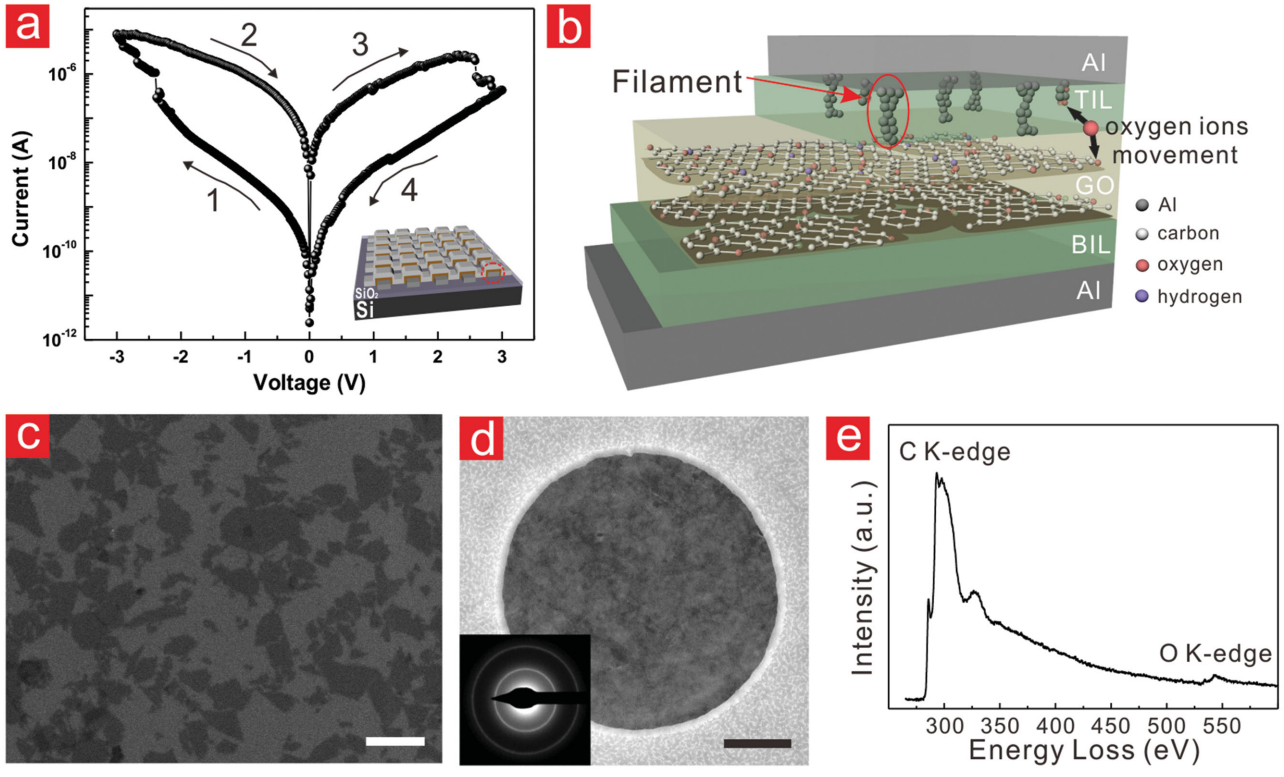

Figure 1. a) Typical *I–V* curve of our Al/GO/Al memory device plotted on a semilogarithmic scale. The bias was applied along the arrows. The inset is a schematic illustration of a GO-based 5 × 5 crossbar memory device. b) A magnified schematic of the red circle in (a). c) SEM image of GO sheets dispersed in DI water (scale bar: 500 nm). d) STEM HAADF image transferred on an Au quantifoil grid (scale bar: 500 nm). The left inset is the electron diffraction pattern of GO films. e) EELS spectra of the C K-edge and O K-edge from GO films.

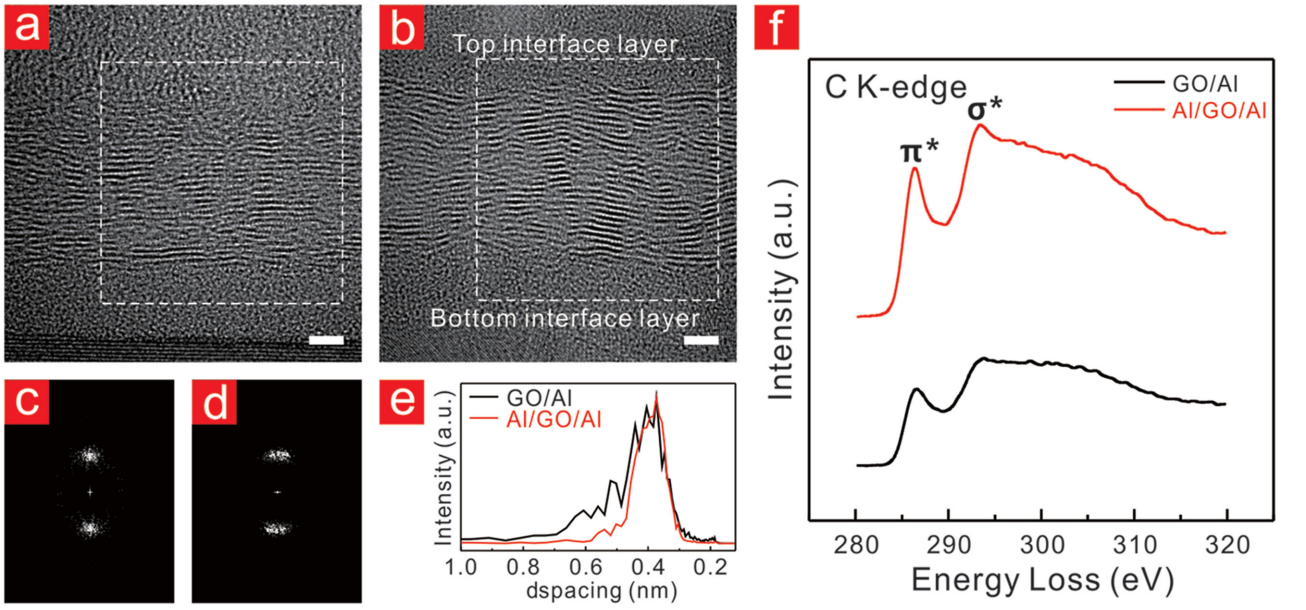

Figure 2. Cross-sectional HRTEM images of GO films on the bottom Al a) before and b) after the top Al deposition (scale bar: 2 nm). (c) and (d) are corresponding FFT patterns obtained in the white rectangular regions of (a) and (b), respectively. e) The intensity profiles in accordance with the interlayer spacing. f) Coreloss-EELS spectra of the C K-edge from GO films.

schematic diagram of the mechanism is illustrated in Figure 1b. The nanoscale metallic filaments are expected to form in a relatively oxygen-deficient region (Al-rich region), as the oxygen ions in the TIL moved to the GO films during the ON process. To demonstrate this switching mechanism, we need to characterize the structural and chemical properties of each OFF and ON state.

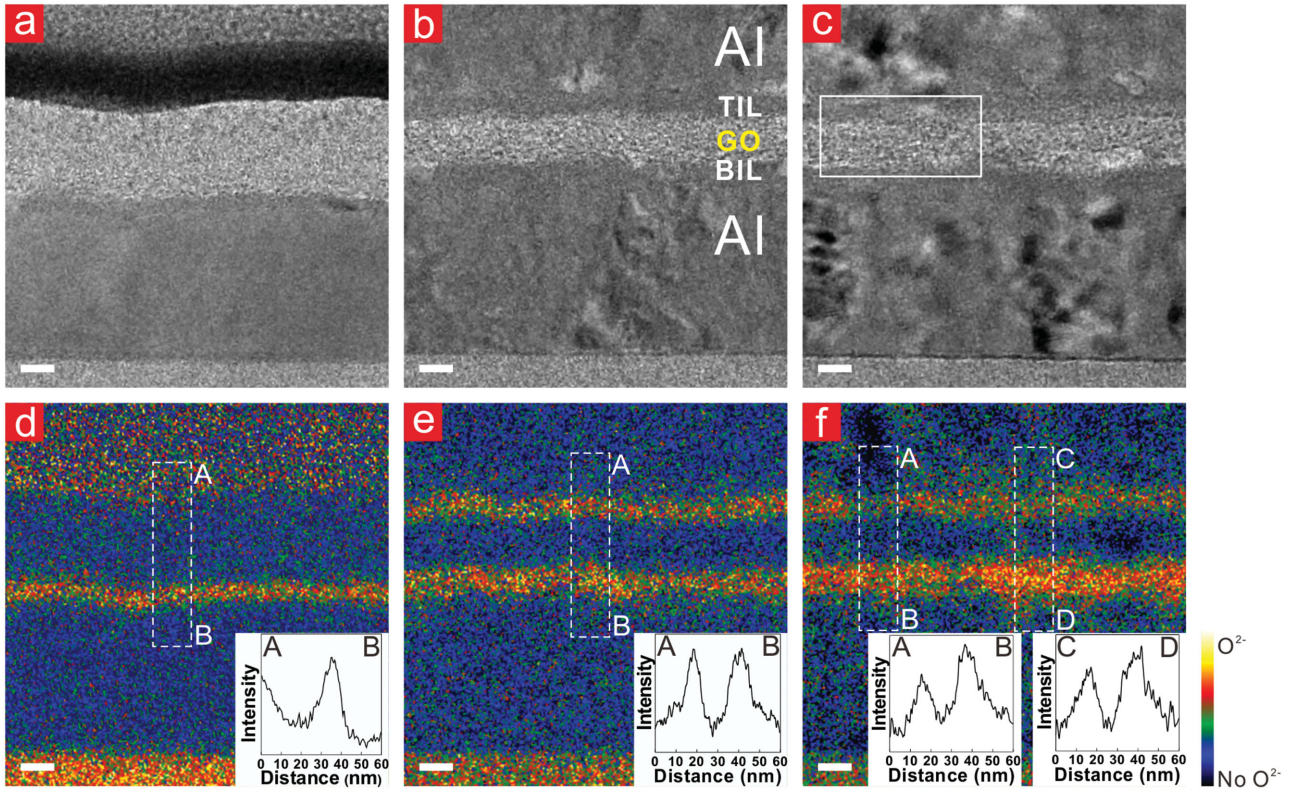

Figure 3. a–c) Energy-filtered TEM zero-loss images and d–f) oxygen elemental maps of three different samples, respectively (scale bar: 10 nm). d) GO films on the bottom Al electrode (pristine state). e) After the top Al electrode deposition (OFF state). f) The device with a negative set bias applied to the top Al electrode (ON state). Each inset shows the average intensity profile obtained from the white rectangular areas.

First, we characterized the properties of GO thin films after the top Al deposition process (OFF state). To reveal these structural and chemical changes, we used a low-voltage aberration-corrected TEM with an operation voltage of 80 kV, because GO can be easily damaged by strong electron beam irradiation. **Figure 2**a,b shows the cross-sectional atomic-resolution TEM images taken before and after the Al top electrode deposition, respectively. Before the Al metal deposition, a GO thin film (≈10 nm thick) was spin-coated on the bottom native aluminum oxide layer. The striped GO sheets were clearly resolved by bright and dark contrasts. It is noticeable that the crystallinity of the GO films increased after Al metal deposition, showing more ordered (0002) lattice fringes. Figure 2c,d shows the FFT patterns obtained from Figure 2a,b, respectively. The bright spot corresponds to the interlayer spacing for the graphitized regions in the GO thin films. The broad spot pattern indicates that the GO films were not perfectly ordered. They included some domains that were slightly rotated to each other and had variant interlayer distances due to the adsorption of the oxygen groups. It is interesting that the FFT spot after Al deposition changed with the different shape of the (0002) spots. While the spot in Figure 2c is round and has broad divergence, the spot in Figure 2d is an arc with small dispersion. This means that the distribution of the interlayer distance between the platelets in the GO films changed. To quantitatively measure the intensity of the spot, the intensity and broadness were analyzed using the ELD program packages provided by Calidris. For the calculation of the RDF from the center to a desired radius, we restricted the range of arc angles to 60° to include all of the bright spot regions. The intensity profiles as a function of the interlayer *d* spacing is shown in Figure 2e. The GO thin films without the Al top electrode show a wide range of *d* spacings. Compared to the GO/Al sample, the Al/GO/Al sample has a narrow profile, which indicates that the GO films were reduced by reacting with the Al top electrode and forming an amorphous TIL.

We also used the EELS spectra of the C K-edge to examine the chemical change in the GO films by the deposition of the Al top electrode (Figure 2f). The intensity of the σ* peak at 293.7 eV in GO/Al is relatively weak because the sp^2 carbon bonding in graphene was converted to sp^3 C–O bonding.[35,36] However, the C–O bond was broken by the movement of oxygen ions to form the TIL, and this induced a sharp σ* peak at 293.4 eV in Al/GO/Al sample. Raman spectra also show the properties of GO thin films by the changes in the relative intensity of the D and G peaks (Figure S5, Supporting Information). In addition, X-ray photoelectron spectroscopy (XPS) and X-ray diffraction (XRD) analyses strongly confirm the reduction of the GO films due to the chemical reaction with the Al metal electrode (Figure S6, Supporting Information).

We next investigated the Al/GO/Al stacked memory cell after the set process (ON state). EFTEM elemental mapping was used to characterize the chemical changes in the trilayers. **Figure 3**a,d shows a zero-loss filtered image and the corresponding oxygen elemental mapping image of the GO/Al sample, respectively. A strong contrast is present on the natively formed bottom interface layer (Al native oxide). Although the contrast is very weak in the region of the GO films, we can identify a small oxygen signal from the average intensity profile in the inset of Figure 3d. Figure 3b,e shows a zero-loss filtered image and the corresponding oxygen mapping image after the Al top electrode deposition. The oxygen ions are mainly distributed on the top and bottom interface, whereas a low oxygen intensity is present in the GO films. As shown in the inset of Figure 3e, the intensity of the oxygen ions in the GO films is lower than that of the oxygen profile in Figure 3d. This might be due to oxygen diffusion into the TIL during Al deposition, as mentioned above. It is worth pointing out that the oxygen distribution remarkably changed after the set process. The oxygen elemental mapping image for the ON state (Figure 3f) shows that the TIL has an uneven oxygen distribution and weaker contrast at a specific local region. The average profile (acquired at the left white rectangle region marked A–B in Figure 3f) clearly indicates that

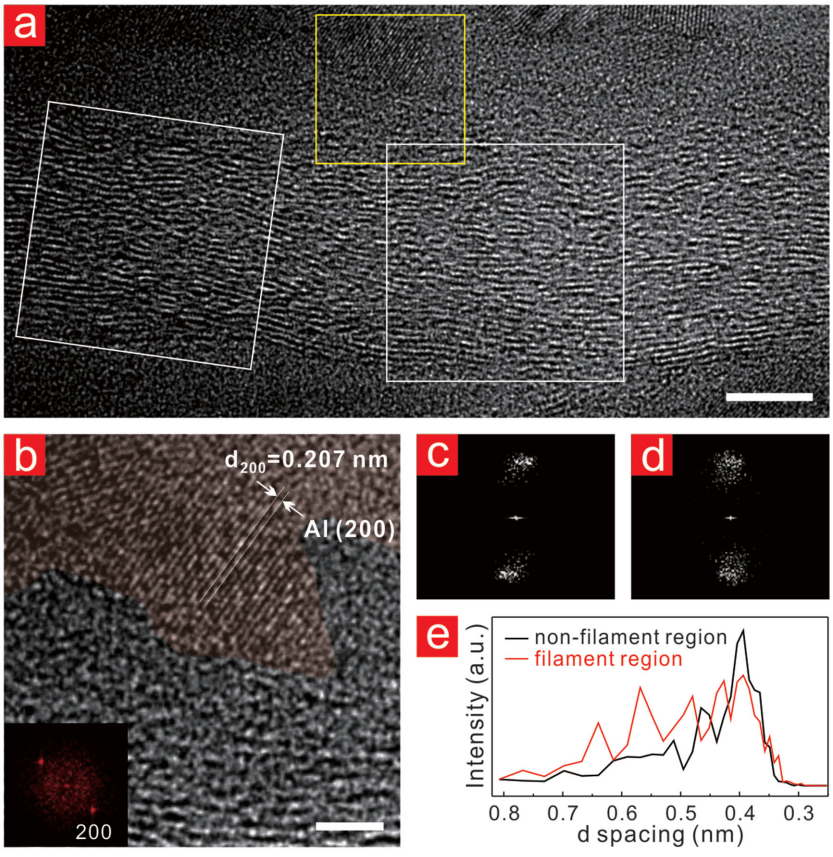

Figure 4. a) Cross-sectional TEM image obtained in the white rectangular region of Figure 3c (scale bar: 5 nm). b) Magnified HRTEM image in the yellow rectangular region of (a). c,d) The FFT patterns obtained from the left and right white rectangular regions of (a), respectively (scale bar: 2 nm). e) The intensity profile of the RDF from the center to a desired radius using the ELD program in the FFTs acquired from (c) and (d). The *x*-axis was represented as a function of the interlayer *d* spacing.

the oxygen-deficient region is locally formed and strongly related to the back-diffusion of oxygen ions into GO thin films. A similar chemical change in the TIL by the movement of oxygen ions can also be observed in another area (Figure S7, Supporting Information). This strongly demonstrates that the local filament was generated by the movement of oxygen ions.

We used the atomic-resolution TEM technique to reveal any microstructural changes in the above oxygen-deficient regions. **Figure 4**a shows a cross-sectional atomic-resolution TEM image of the region marked with a white rectangle in Figure 3c. The crystalline phase is observed with clear lattice fringes in the local region at the amorphous TIL. The spacing of the fringes corresponds to the interplanar spacing of (200) planes in the Al metal phase. We note that the shape of the crystalline phase is like a protrusion grown on the surface of the TIL. This strongly suggests that the Al ion-rich (oxygen-deficient) area is formed by the back-diffusion of oxygen ions into GO films during the application of a negative bias to the top electrode. In this way, the Al metal crystalline can be grown from the TIL and connected to the GO films, creating an electrical conduction path in the TIL (Figure 4b). The corresponding change in the GO films can also be observed. An HRTEM image of the GO films obtained in the below region with the Al metallic phase (the right white rectangle area) shows a much more disordered structure than that of the left rectangle region (which does not have a metallic phase in the TIL). Results from a quantitative analysis using an FFT obtained from two HRTEM images of GO films are shown in Figure 2c–e. The GO films faced with an Al metallic phase at the TIL show a round spot and an increased interlayer spacing of (0002). This can be explained by oxygen back-diffusion into the GO films, again leading to C–O bonding. The HRTEM image in the left white rectangle in Figure 4a is similar to that of the OFF state shown in Figure 2b. This indicates that the oxygen ions diffuse in the local area and put the device in the ON state by inducing a local filamentary path.

The schematic in **Figure 5** shows the resistive switching mechanism of GO-based memory based on the above experimental results. GO sheets decorated with various oxygen groups are stacked randomly on the Al bottom electrode. An amorphous TIL is inevitably formed through the chemical reaction with Al metal and oxygen ions within GO thin films. This reaction results in a decrease in the interlayer spacing of graphene sheets due to the desorption of oxygen ions. Meanwhile, the amorphous TIL plays a crucial role in controlling the total resistance of Al/GO/Al memory cells, placing the cell in the OFF state. The application of a negative bias breaks the Al–O chemical bonds during the set process, and oxygen ions diffuse into the GO films. Oxygen ions are relatively deficient in the local TIL where a strong field is locally induced; this simultaneously results in an Al-rich region in the TIL and a disordered area in the GO films. The Al-rich region can be crystallized along the top Al metal grains. It propagates to near the GO films and the metallic conducting filaments decrease the total resistance, placing the cell in the ON state.

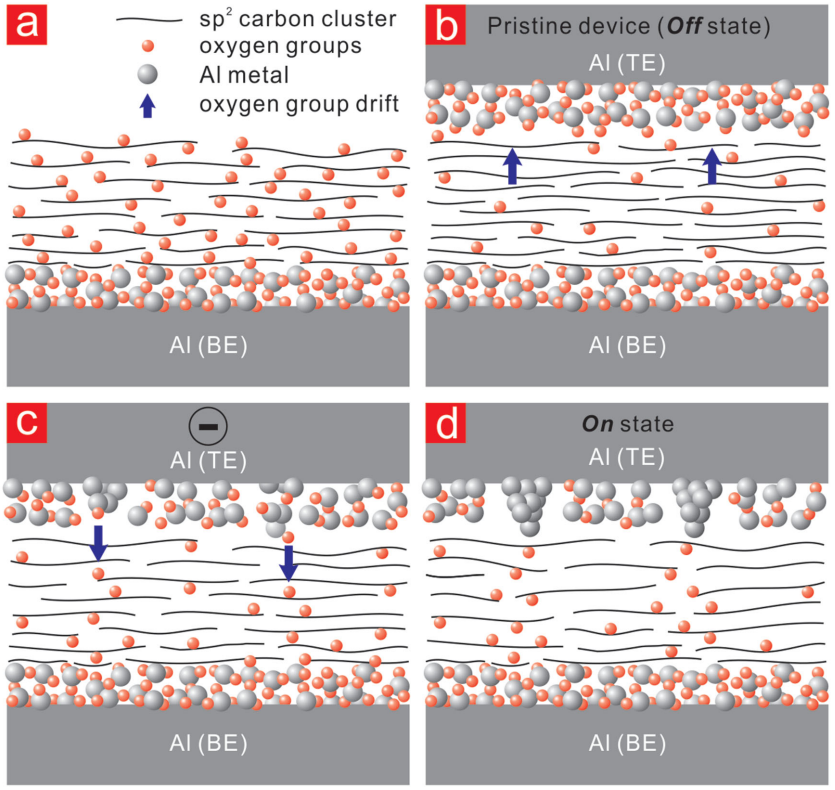

Figure 5. Schematic showing the formation process of local metallic filaments within the amorphous TIL. a) GO thin films on the bottom electrode. b) The pristine Al/GO/Al device after top Al deposition. c) Oxygen-ion diffusion into the GO films by an external negative bias on the top electrode. d) The ON state after applying a negative bias to the top electrode. The formation of the Al crystalline and the change in the interlayer spacing of the GO films due to oxygen migration are shown.

3. Conclusions

In summary, we have demonstrated that the formation of Al metallic nanocrystal within the TIL, which is induced by the movement of oxygen ions into GO thin films, can be attributed to the microscopic origin of the bistable resistive switching behaviors of our Al/GO/Al memory devices. From cross-sectional atomic-resolution TEM images and a quantitative analysis of the corresponding FFT patterns, we showed that the GO thin films are reduced and ordered by the desorption of oxygen ions after Al top electrode deposition. The EFTEM oxygen mapping and atomic-resolution TEM images of a sample in the ON state clearly show the formation of an oxygen-deficient region at the amorphous TIL and the growth of Al metallic filaments from the top Al surface. These contribute to the electrical conducting path in an Al/GO/Al memory device. Our findings provide crucial evidence to explain interface-dominant switching models in GO-based resistive memory.

4. Experimental Section

Synthesis of GO: Graphene oxide was synthesized from natural graphite (Graphi Kropfmühl AG, MGR 25 998 K) using the modified Hummers method. Graphite powder was sonicated for 2 h in water to achieve exfoliated GO sheets. The slurry of GO was centrifuged at 15 000 rpm for 20 min (Hanil Supra 22 K) to remove unexfoliated particles. The supernatant contained ≈2 wt% of GO.

Device Fabrication: Al/GO/Al devices were fabricated by the following process. Al bottom electrode lines, 50 nm thick and 60 μm wide, were deposited onto an SiO_2 substrate using an overlapped shadow mask using electron beam evaporation. Before deposition, the substrate with patterned Al electrode lines was subjected to a UV–ozone plasma step for 5 min due to the surface treatment and cleaning. The GO solution was spread onto the patterned substrate using a spin-coating method, and it was baked at 100 °C for 30 min. Lastly, the Al top electrode, crossing the bottom electrode at an angle of 90°, was deposited on the GO films by electron beam evaporation.

Materials Characterization: The electrical properties of devices were characterized using a Keithley-4200 semiconductor parameter analyzer under ambient conditions. TEM images were taken by a FEI Titan^3 G2 60–300 with an image-forming Cs corrector at an accelerating voltage of 80 kV. The cross-sectional TEM samples of memory cells were prepared using a focused ion beam (FIB, FEI Helios Nano Lab 450) and were additionally thinned by a low-energy Ar-ion milling system (Fischione Model 1040 Nanomill). EELS spectra and EFTEM elemental mapping were recorded using a Gatan Imaging Filter. SEM images of GO nanosheet images were obtained using a FEI Verios 460 with an accelerating voltage of 10 kV. FTIR spectra were obtained using a Nicolet iS50 FT-IR spectrometer. XPS measurements were performed on a Sigma Probe (Thermo VG Scientific). The Raman spectra were obtained using an ARAMIS (Horiba Jobin Yvon, France). XRD patterns were characterized using a RIGAKU Ultima IV (fixed θ method).

Supporting Information

Supporting Information is available from the Wiley Online Library or from the author.

Acknowledgements

This work was supported by Basic Science Research Program through the National Research Foundation of Korea (NRF) funded by the Ministry of Education (NRF-2014R1A1A2058713), UNIST (1.120032.01), the Global Frontier Research Center for Advanced Soft Electronics (2011-0031640), and also by IBS-R004-G3.

Received: July 4, 2015
Revised: August 25, 2015
Published online: October 15, 2015

[1] R. Waser, M. Aono, *Nat. Mater.* **2007**, *6*, 833.
[2] A. Sawa, *Mater. Today* **2008**, *11*, 28.
[3] M.-J. Lee, S. Han, S. H. Jeon, B. H. Park, B. S. Kang, S.-E. Ahn, K. H. Kim, C. B. Lee, C. J. Kim, I.-K. Yoo, D. H. Seo, X.-S. Li, J.-B. Park, J.-H. Lee, Y. Park, *Nano Lett.* **2009**, *9*, 1476.
[4] D.-H. Kwon, K. M. Kim, J. H. Jang, J. M. Jeon, M. H. Lee, G. H. Kim, X.-S. Li, G.-S. Park, B. Lee, S. Han, M. Kim, C. S. Hwang, *Nat. Nanotechnol.* **2010**, *5*, 148.
[5] M.-J. Lee, C. B. Lee, D. Lee, S. R. Lee, M. Chang, J. H. Hur, Y.-B. Kim, C.-J. Kim, D. H. Seo, S. Seo, U. I. Chung, I.-K. Yoo, K. Kim, *Nat. Mater.* **2011**, *10*, 625.
[6] Y. C. Yang, F. Pan, Q. Liu, M. Liu, F. Zeng, *Nano Lett.* **2009**, *9*, 1636.
[7] Z. Wang, H. Yu, X. A. Tran, Z. Fang, J. Wang, H. Su, *Phys. Rev. B* **2012**, *85*, 195322.
[8] Y. Yang, W. Lu, Y. Yao, J. Sun, C. Gu, L. Gu, Y. Wang, X. Duan, R. Yu, *Sci. Rep.* **2014**, *4*, 3890.
[9] S.-J. Choi, G.-S. Park, K.-H. Kim, S. Cho, W.-Y. Yang, X.-S. Li, J.-H. Moon, K.-J. Lee, K. Kim, *Adv. Mater.* **2011**, *23*, 3272.
[10] T.-W. Kim, H. Choi, S.-H. Oh, G. Wang, D.-Y. Kim, H. Hwang, T. Lee, *Adv. Mater.* **2009**, *21*, 2497.
[11] Y. Yang, P. Gao, S. Gaba, T. Chang, X. Pan, W. Lu, *Nat. Commun.* **2012**, *3*, 732.
[12] T. Rueckes, K. Kim, E. Joselevich, G. Y. Tseng, C.-L. Cheung, C. M. Lieber, *Science* **2000**, *289*, 94.
[13] S. K. Hwang, J. M. Lee, S. Kim, J. S. Park, H. I. Park, C. W. Ahn, K. J. Lee, T. Lee, S. O. Kim, *Nano Lett.* **2012**, *12*, 2217.
[14] F. Kreupl, R. Bruchhaus, P. Majewski, J. B. Philipp, R. Symanczyk, T. Happ, C. Arndt, M. Vogt, R. Zimmermann, A. Buerke, *IEDM* **2009**, 521.
[15] F. Zhuge, W. Dai, C. L. He, A. Y. Wang, Y. W. Liu, M. Li, Y. H. Wu, P. Cui, R.-W. Li, *Appl. Phys. Lett.* **2010**, *96*, 163505.
[16] Y.-J. Chen, H.-L. Chen, T.-F. Young, T.-C. Chang, T.-M. Tsai, K.-C. Chang, R. Zhang, K.-H. Chen, J.-C. Lou, T.-J. Chu, J.-H. Chen, D.-H. Bao, S. Sze, *Nanoscale Res. Lett.* **2014**, *9*, 1.
[17] O. C. Compton, S. T. Nguyen, *Small* **2010**, *6*, 711.
[18] J. Liu, Z. Yin, X. Cao, F. Zhao, L. Wang, W. Huang, H. Zhang, *Adv. Mater.* **2013**, *25*, 233.
[19] C. Wu, F. Li, Y. Zhang, T. Guo, T. Chen, *Appl. Phys. Lett.* **2011**, *99*, 042108.
[20] A.-D. Yu, C.-L. Liu, W.-C. Chen, *Chem. Commun.* **2012**, *48*, 383.
[21] S. Myung, J. Park, H. Lee, K. S. Kim, S. Hong, *Adv. Mater.* **2010**, *22*, 2045.
[22] Z. Yin, Z. Zeng, J. Liu, Q. He, P. Chen, H. Zhang, *Small* **2013**, *9*, 727.
[23] S. K. Hong, J. E. Kim, S. O. Kim, S.-Y. Choi, B. J. Cho, *IEEE Electro. Device L.* **2010**, *31*, 1005.
[24] F. Zhuge, B. Hu, C. He, X. Zhou, Z. Liu, R.-W. Li, *Carbon* **2011**, *49*, 3796.
[25] L.-H. Wang, W. Yang, Q.-Q. Sun, P. Zhou, H.-L. Lu, S.-J. Ding, D. Wei Zhang, *Appl. Phys. Lett.* **2012**, *100*, 063509.
[26] S. K. Hong, J. E. Kim, S. O. Kim, B. J. Cho, *J. Appl. Phys.* **2011**, *110*, 044506.
[27] D. Y. Yun, T. W. Kim, *Carbon* **2015**, *88*, 26.
[28] S. Porro, E. Accornero, C. F. Pirri, C. Ricciardi, *Carbon* **2015**, *85*, 383.
[29] H. Y. Jeong, J. Y. Kim, J. W. Kim, J. O. Hwang, J.-E. Kim, J. Y. Lee, T. H. Yoon, B. J. Cho, S. O. Kim, R. S. Ruoff, S.-Y. Choi, *Nano Lett.* **2010**, *10*, 4381.
[30] D. A. Dikin, S. Stankovich, E. J. Zimney, R. D. Piner, G. H. B. Dommett, G. Evmenenko, S. T. Nguyen, R. S. Ruoff, *Nature* **2007**, *448*, 457.
[31] D. C. Marcano, D. V. Kosynkin, J. M. Berlin, A. Sinitskii, Z. Sun, A. Slesarev, L. B. Alemany, W. Lu, J. M. Tour, *ACS Nano* **2010**, *4*, 4806.
[32] W. S. Hummers, R. E. Offeman, *J. Am. Chem. Soc.* **1958**, *80*, 1339.
[33] A. Allain, Z. Han, V. Bouchiat, *Nat. Mater.* **2012**, *11*, 590.
[34] C. Gómez-Navarro, J. C. Meyer, R. S. Sundaram, A. Chuvilin, S. Kurasch, M. Burghard, K. Kern, U. Kaiser, *Nano Lett.* **2010**, *10*, 1144.
[35] K. A. Mkhoyan, A. W. Contryman, J. Silcox, D. A. Stewart, G. Eda, C. Mattevi, S. Miller, M. Chhowalla, *Nano Lett.* **2009**, *9*, 1058.
[36] A. Dato, M. Frenklach, *New J. Phys.* **2010**, *12*, 125013.